Journal of Materials Chemistry A

ROYAL SOCIETY OF CHEMISTRY

PAPER

View Article Online
View Journal | View Issue

Check for updates

Cite this: *J. Mater. Chem. A*, 2026, **14**, 8232

Over 50 wt% loaded nanoparticulate Ru on hollow carbon spheres as efficient catalysts for the conversion of levulinic acid to γ-valerolactone under ambient conditions

Yeon Seo Kong,† Rakesh Parida,† Yoon Kee Kim, Hyun Su Kim, Jin Yong Lee * and Seung Uk Son *

Received 9th November 2025
Accepted 12th January 2026

DOI: 10.1039/d5ta09104g

rsc.li/materials-a

The conversion of biomass-derived levulinic acid (LA) to γ-valerolactone (GVL) is one of the key transformations for producing bio-fuel precursors. Although various Ru-based heterogeneous catalysts have been developed, these conversions typically required 0.25–2.8 mol% Ru for LA, high temperatures (~150 °C), and high H_2 pressures (up to 50 bar). To enable more sustainable GVL production under milder reaction conditions, the development of more efficient catalysts is required. In this work, Ru nanoparticles supported on the hollow carbon spheres (Ru/HC) were successfully engineered using hollow microporous organic polymers (HMOPs) as templates. In particular, the coating of tannic acid on the HMOP facilitated the efficient incorporation of Ru species into the templating materials. The optimized 51.6 wt% Ru/HC-3 catalyst with 0.25 mol% Ru for LA exhibited excellent catalytic performance, achieving a 94% GVL yield and good recyclability at 100 °C under 5 bar H_2. The excellent catalytic performance of Ru/HC-3 under mild conditions can be attributed to the unusually low reduction temperature (80 °C) of the surface RuO_x species.

Introduction

For the sustainable production of value-added chemicals and the realization of a resilient society in the face of climate change, the exploration of alternatives to petroleum-based resources has become increasingly crucial.[1] In this context, the chemical conversion of biomass, primarily derived from plant materials, has recently attracted significant attention.[2] In particular, the selective transformation of biomass into valuable platform chemicals is of great practical importance.[3]

From a chemical perspective, the cell wall is a major component of biomass, composed mainly of lignocellulosic material.[4] Among its three principal constituents, cellulose has been most extensively studied for producing platform chemicals. Acid-catalyzed hydrolysis of cellulose yields glucose, which can be isomerized to fructose and then dehydrated to form the key platform compound 5-hydroxymethylfurfural (HMF).[5]

Levulinic acid (LA), identified by the U.S. DOE as a top value-added chemical from biomass, can be produced *via* hydration of HMF.[6] Tandem hydrogenation and dehydration of LA affords γ-valerolactone (GVL), a promising biofuel precursor (Fig. 1).[7] Recently, Ru-based catalysts have been extensively studied for this transformation, typically supported on carbon materials or metal oxides (TiO_2, ZrO_2, SiO_2, and Al_2O_3) with Ru loadings of 0.37–8.6 wt%.[8–10] To the best of our knowledge, achieving Ru loadings above 10 wt% on solid supports remains challenging, as excessive loading can cause aggregation and reduce catalytic performance.

Achieving GVL with high selectivity (>90% yields) over Ru-based catalysts typically requires 0.25–2.8 mol% Ru for LA, elevated temperatures (150–200 °C), and high H_2 pressures (30–

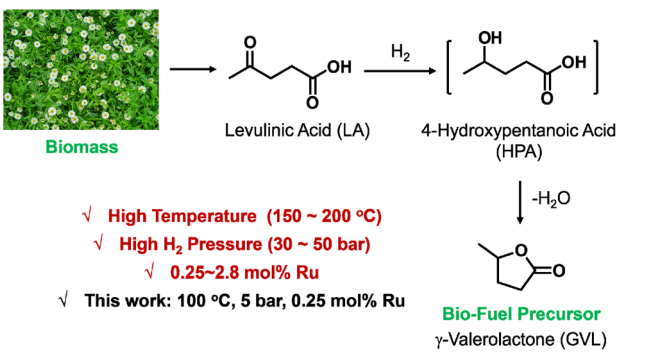

Fig. 1 Chemical conversion of biomass-derived levulinic acid to γ-valerolactone, along with the conventional reaction conditions for Ru-catalyzed systems reported in the literature.[8–10]

Department of Chemistry, Sungkyunkwan University, Suwon 16419, Korea. E-mail: sson@skku.edu; jinylee@skku.edu

† These authors contributed equally to this work.

50 bar), resulting in increased energy consumption and the need for specialized equipment (Fig. 1 and Table S1 in the SI).[8–10] For more sustainable GVL production, efficient catalytic systems operating under milder temperatures and lower H_2 pressures are desirable.

Various heterogeneous inorganic catalysts have been developed for biomass conversion to chemicals.[11] To enhance catalytic performance, the nanoscale structures of these catalysts have been engineered using template methods.[12] For example, porous organic templates can incorporate inorganic precursors, which upon thermolysis generate metal nanoparticles supported on carbon materials. Hollow nanocatalysts can be further fabricated by removing the inner templating material.[13] Since catalytic reactions occur primarily on the surface of heterogeneous catalysts, the inner components of bulk materials are often underutilized. Therefore, engineering hollow structures can improve catalytic performance by maximizing surface accessibility.[13]

Recently, microporous organic polymers (MOPs) have been synthesized *via* the coupling of organic building blocks.[14] The micropores of MOPs provide sites for the incorporation of catalyst precursors.[15] Moreover, hollow morphologies of MOPs can be constructed *via* template-assisted approaches to enhance mass transport and surface accessibility.[16] Due to their organic nature, MOPs are generally nonpolar and hydrophobic. Conventional MOP powders prepared *via* Sonogashira coupling of organic building blocks float on water (Fig. 2a). While nonpolar precursors such as organometallic compounds can be well incorporated into MOPs,[17] conventional metal halides are inefficient due to their polar nature (Fig. 2a). Therefore, to enable incorporation of metal halide precursors, the chemical properties of MOPs must be post-modified.

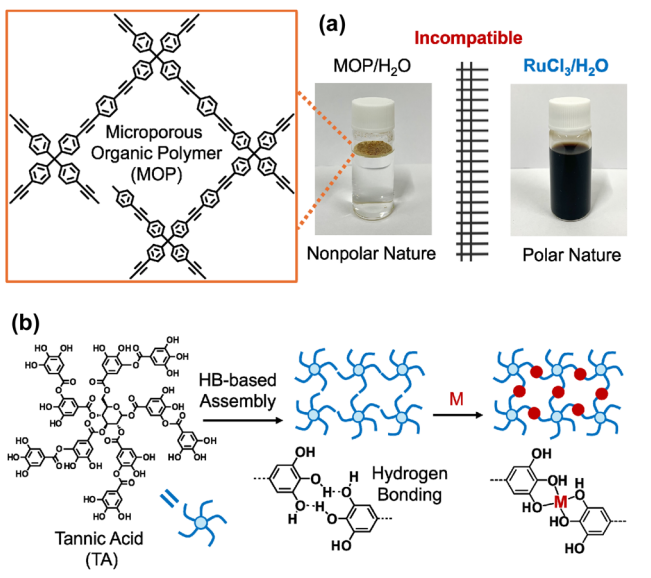

Fig. 2 (a) Comparison of the nonpolar nature of MOP in water with the polar nature of $RuCl_3$. (b) Chemical structure of tannic acid (TA), its assembly *via* hydrogen bonding, and its facile coordination to metal ions.

Tannic acid (TA) is a versatile compound rich in hydrophilic galloyl groups (Fig. 2b).[18] Owing to the facile formation of intermolecular hydrogen bonds between galloyl groups, TA can be used to coat solid materials.[19] Moreover, various metal ions can be incorporated into the assembled TA networks *via* coordination with hydroxyl groups and various metal–TA networks have been reported.[20] Therefore, TA can potentially be employed to modify the surface properties of MOPs, rendering them polar and facilitating the incorporation of polar metal halide precursors. The combination of MOP materials with TA chemistry thus provides a promising approach for preparing precursor materials for the synthesis of metals on carbon supports.

In this work, we report the engineering of Ru nanoparticles loaded on hollow carbon spheres (Ru/HCs) using TA-modified hollow microporous organic polymer (HMOP@TA) templates and their catalytic performance in the conversion of LA to GVL under mild conditions.

Experimental section

General information

Transmission electron microscopy (TEM) and energy dispersive X-ray spectroscopy (EDS)-based elemental mapping studies were conducted using a JEM2100F microscope. High-resolution (HR)-TEM analysis was conducted using a JEM ARM 200F microscope. N_2 adsorption–desorption isotherm curves were obtained at 77 K using a Micromeritics ASAP 2020 instrument and analyzed by the Brunauer–Emmett–Teller (BET) theory. Pore size distribution analysis of materials was conducted by the nonlocal-density functional theory (NL-DFT) method. Water contact angles (WCAs) were measured using a Theta Optical Tensiometer (KSV Instruments, Ltd). Solid state ^{13}C nuclear magnetic resonance (NMR) spectra were obtained using a 500 MHz Bruker ADVANCE III HD spectrometer at the National Center for Inter-University Research Facilities of Seoul National University of Korea. Infrared (IR) spectra were obtained using a Bruker VERTEX 70 spectrometer at the Chiral Material Core Facility Center of Sungkyunkwan University. Powder X-ray diffraction (PXRD) patterns were obtained using Rigaku Ultima IV equipment. X-ray photoelectron spectra (XPS) were obtained using a Thermo VG Spectrometer. Combustion elemental analysis was conducted using a FLASH 2000 analyzer. Thermogravimetric analysis (TGA) curves were obtained using SDT 650 equipment. Inductively coupled plasma-atomic emission spectroscopy (ICP-AES) was conducted using OPTIMA 8300 equipment. H_2-temperature-programmed reduction (TPR) and temperature-programmed desorption (TPD) studies of materials were conducted using AutoChem II 2920 V 4.03 equipment. For the H_2-TPR studies, the samples were pretreated at 150 °C under Ar for 1 h and then were analyzed in the temperature range of 50–600 °C under 10% H_2/Ar gas with a temperature increase rate of 10 °C min^{-1}. For the H_2-TPD studies, the samples were pretreated at 400 °C for 2 h under 10% H_2/Ar gas, cooled to 50 °C, purged with Ar gas for 1 h, and then, analyzed in the temperature range of 50–900 °C under 10% H_2/Ar gas with a temperature increase rate of 10 °C min^{-1}. Conventional

solution-based ^{1}H and ^{13}C NMR spectra were obtained using a Bruker Ascend 500 MHz spectrometer at the Chiral Material Core Facility Center of Sungkyunkwan University. High resolution-mass spectroscopy (HR-MS) was conducted using a Xevo G2-XS-UPC2 spectrometer at the Chiral Material Core Facility Center, Sungkyunkwan University.

Synthesis of HMOP and HMOP@TA

Silica nanospheres were prepared by the Stöber method reported in the literature.[21] In this work, the following synthetic procedures were applied. Ethanol (200 mL), distilled water (8 mL), and a spin bar were added to a 250 mL round-bottomed flask under air. After ammonia solution (25–30%, 4 mL) was added, the flask was sealed with a rubber septum. After stirring at room temperature for 1 h, tetraethyl orthosilicate (TEOS, 14 mL) was quickly added. The mixture was stirred at room temperature for 18 h. A half portion (~113 mL) of the reaction mixture was transferred to hexane (300 mL) in a 500 mL Erlenmeyer flask. After seven drops of acetic acid (99.5%) were added, the flask was shaken. After the suspension was transferred to a 50 mL Falcon tube, the silica powders were separated by centrifugation, washed with a mixture of methanol (20 mL) and acetone (20 mL) three times, and dried under vacuum. The other half portion was treated by the same procedures. To remove organic residues, the silica spheres were calcined in a furnace at 550 °C for 4 h under air.

For the preparation of HMOP, silica spheres (0.50 g), $(PPh_3)_2PdCl_2$ (14 mg, 20 μmol), CuI (3.8 mg, 20 μmol), distilled triethylamine (40 mL), and distilled toluene (10 mL) were added to a flame-dried 100 mL two-necked Schlenk flask under argon. The reaction mixture was sonicated at room temperature for 1 h. After tetra(4-ethynylphenyl)methane (83 mg, 0.20 mmol) and 1,4-diiodobenzene (0.132 g, 0.400 mmol) in toluene (10 mL) were added, the reaction mixture was stirred at 80 °C for 24 h. After cooling to room temperature, the solid (MOP@SiO_2) was separated by centrifugation, washed with methylene chloride (50 mL) once, methanol (50 mL) once, and acetone (50 mL) once, and dried under vacuum. MOP@SiO_2 was added to a mixture of hydrofluoric acid (48–51%, 10 mL), distilled water (10 mL), and methanol (25 mL) in a 50 mL Falcon tube. **Caution**: the hydrofluoric acid is extremely toxic and should be handled with specific gloves in a hood. After the reaction mixture was stirred at room temperature for 4 h, the solid (HMOP) was separated by centrifugation, washed with a mixture of water (20 mL) and methanol (25 mL) four times, and dried under vacuum. **Caution**: the excess HF residues were neutralized with aqueous NaOH solution.

For the preparation of HMOP@TA, HMOP (25 mg), distilled water (12.5 mL), and ethanol (12.5 mL) were added to a 50 mL Falcon tube. The mixture was sonicated at room temperature for 1 h. After tannic acid (0.40 g, 0.20 mmol) was dissolved in a mixture of distilled water (12.5 mL) and ethanol (12.5 mL), it was added to the reaction mixture. After the reaction mixture was vortexed at room temperature for 30 s, the solid (HMOP@TA) was separated by centrifugation, transferred to a 10 mL vial, washed with water (10 mL) three times, and dried under vacuum.

Synthesis of Ru/HC-1–3 and control Ru/C (C–Ru)

For the preparation of Ru/HC-3, HMOP@TA (10 mg) and ethyl acetate (5 mL) were added to a flame-dried 50 mL two-necked Schlenk flask and the mixture was sonicated at room temperature for 5 min. After $RuCl_3 \cdot H_2O$ (40 mg, 0.19 mmol) was dissolved in ethyl acetate (5 mL) by sonication, it was added to the HMOP@TA suspension. The reaction mixture was stirred at 90 °C for 6 h. After cooling to room temperature, the solid (HMOP@TA–Ru) was separated by centrifugation, transferred to a 10 mL vial, washed with ethyl acetate (10 mL) three times, and dried under vacuum. The HMOP@TA–Ru was treated at 500 °C for 4 h under argon in a furnace to form Ru/HC-3. For the preparation of Ru/HC-1, the same procedures as those of Ru/HC-3 were applied except that $RuCl_3 \cdot H_2O$ (5 mg, 24 μmol) was used. For the preparation of Ru/HC-2, the same procedures as those of Ru/HC-3 were applied except using $RuCl_3 \cdot H_2O$ (10 mg, 48 μmol). For the preparation of control Ru/C (C–Ru), the same procedures as those of Ru/HC-3 were applied except that HMOP was used instead of HMOP@TA.

TGA in air indicated 28.5, 44.5, 68.0, and 65.7 wt% residues for Ru/HC-1, Ru/HC-2, Ru/HC-3, and C–Ru, respectively, corresponding to 21.6, 33.8, 51.6, and 49.9 wt% Ru. Based on these results, the Ru contents in Ru/HC-1, Ru/HC-2, Ru/HC-3, and C–Ru were analyzed to be 2.14, 3.34, 5.11, and 4.94 mmol Ru per g, respectively. It is noteworthy that metallic Ru is poorly soluble even in aqua regia,[22] and thus, TGA in air has been used for quantitative analysis of Ru in carbon materials.[23]

Experimental procedures of catalytic reactions

For the catalytic reaction, after levulinic acid (0.204 mL, 2.00 mmol), Ru/HC (0.25 mol% Ru relative to LA, the contents of Ru in each catalyst: 2.14 mmol Ru per g for Ru/HC-1, 3.34 mmol Ru per g for Ru/HC-2, 5.11 mmol Ru per g for Ru/HC-3, 4.94 mmol Ru per g for control Ru/C), water (2 mL), and a spin bar were added to an autoclave, the setup was assembled. After H_2 gas was purged for 30 s, the autoclave was charged with 5 bar H_2 gas. The reaction mixture was stirred at 100 °C for 2 h. After cooling using an ice bath, the excess H_2 gas was vented. The crude products were analyzed by ^{1}H NMR using maleic acid (2.00 mmol) as an internal standard. For the recyclability tests, after the reaction mixture was transferred to an 8 mL vial, the Ru/HC-3 catalyst was separated by centrifugation, washed with water three times, dried under vacuum, and used for the next run.

For the isolation of GVL from the reaction mixture, the following procedures were applied. First, the Ru/HC-3 catalyst was removed by filtration with a syringe filter. Using 1 M $NaHCO_3$ solution, the pH of aqueous product solution was set to 9. Under basic conditions, the HPA intermediate became water soluble while GVL is very soluble in organic media. The GVL was extracted with ethyl acetate three times and dried using $MgSO_4$. After evaporation of volatile solvent, the pure GVL was obtained. ^{1}H and ^{13}C NMR spectra of isolated GVL matched

well with those reported in the literature.[24] Characterization data of GVL: isolated yield of 91%, ^{1}H NMR (500 MHz, $CDCl_3$) $\delta = 4.64$ (m, 1H), 2.55 (m, 2H), 2.36 (m, 1H), 1.83 (m, 1H), 1.41 (d, $J = 6.3$ Hz, 3H) ppm, ^{13}C NMR (125 MHz, $CDCl_3$) $\delta = 177.3$, 76.9, 29.9, 29.2, 21.2 ppm, HR-MS (ESI): $[M + H]^+$ for $C_5H_8O_2$ calc. 101.0597, found 101.0603.

Procedures of computational studies

To evaluate the catalytic activity of the Ru(002) surface for the conversion of levulinic acid (LA) to γ-valerolactone (GVL), density functional theory (DFT) calculations were carried out using the Vienna *Ab initio* Simulation Package (VASP).[25] The Projector Augmented-Wave (PAW) method was employed to describe the interaction between core and valence electrons. Structural optimizations were performed using the Perdew–Burke–Ernzerhof (PBE) functional[26] within the framework of the generalized gradient approximation (GGA) to accurately capture exchange–correlation effects. To properly account for long-range dispersion effects, Grimme's DFT-D3 [27] correction was incorporated, and spin-polarization was considered. To construct the catalytic model, the Ru unit cell was first optimized, yielding lattice constants of $a = b = 2.71$ Å, which are in good agreement with the reported experimental values. Based on this, a Ru(002) surface was modeled as a periodic 5 × 5 slab consisting of four atomic layers, separated by a 15 Å vacuum to eliminate interactions between the slab and its periodic image along the direction perpendicular to its surface plane. During structural optimization, the bottom two layers were fixed to simulate the bulk structure, while the upper two layers were fully relaxed. Geometry optimizations were performed using a Γ-centered *k*-point mesh of 2 × 2 × 1 for Brillouin zone sampling. The plane-wave energy cutoff was set to 400 eV, with convergence thresholds of 10^{-4} eV for total energy and 0.02 eV Å^{-1} for atomic forces.

The adsorption energies (E_{ads}) of the key intermediates involved in the catalytic conversion of LA to GVL on the Ru(002) surface were calculated using the following equation: $E_{ads} = E_{Ru(002)+substrate} - (E_{Ru(002)} + E_{substrate})$, $E_{Ru(002)+substrate}$ is the total energy of the Ru(002)–substrate (LA, HPA, or GVL) system, $E_{Ru(002)}$ denotes the energy of the clean Ru(002) surface, and $E_{substrate}$ represents the energy of the isolated LA, HPA, or GVL molecule in the gas phase.

Results and discussion

Fig. 3 illustrates the synthetic route for HMOP@TA and Ru/HCs. First, HMOP was prepared using silica nanospheres as templates.[21] In the presence of silica spheres, the Sonogashira coupling of 1 eq. tetra(4-ethynylphenyl)methane with 2 eq. 1,4-diiodobenzene yielded MOP-coated silica spheres (SiO_2@MOP). Subsequent etching of inner silica with aqueous HF solution resulted in HMOP.[28] Treatment of HMOP with TA in a mixture of water and ethanol led to the formation of a TA coating on the HMOP materials *via* intermolecular hydrogen bonding between galloyl groups.

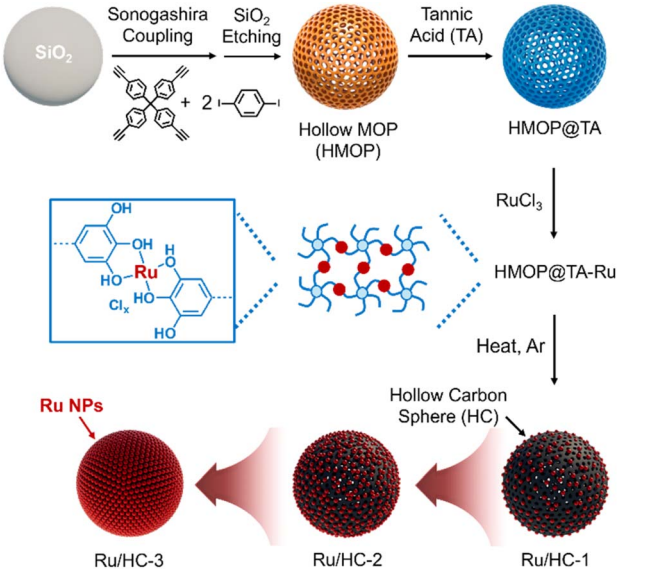

Fig. 3 Synthetic scheme of Ru nanoparticles supported on hollow carbon spheres (Ru/HCs).

The reaction of HMOP@TA with $RuCl_3$ in ethyl acetate facilitated the incorporation of Ru through coordination with polar phenolic groups, producing HMOP@TA–Ru. Thermolysis of HMOP@TA–Ru under an argon atmosphere generated Ru/HCs. By keeping the amount of HMOP@TA templates constant, the loading of $RuCl_3$ precursor was systematically varied from 24 μmol to 48 and 192 μmol, resulting in a series of catalysts denoted as Ru/HC-1, Ru/HC-2, and Ru/HC-3, respectively. For comparison, C–Ru materials were prepared using the same synthetic procedure as Ru/HC-3, but employing HMOP instead of HMOP@TA.

The morphologies and sizes of the materials were analyzed by TEM (Fig. 4). Compared to the inner dark contrast of silica nanospheres, HMOP exhibited a hollow structure with a brighter inner contrast (Fig. 4a and b). The diameter and shell thickness of HMOP were determined to be 213 ± 9 nm and 18 ± 2 nm, respectively (Fig. 4b). Upon incorporation of TA into the micropores of the HMOP shells, the resultant HMOP@TA showed a slightly increased diameter of 220 ± 11 nm and a shell thickness of 23 ± 2 nm (Fig. 4c).

Ru/HC-1–3 retained the original hollow structures of the HMOP@TA templates (Fig. 4d–f). The diameters of Ru/HC-1, Ru/HC-2, and Ru/HC-3 gradually increased from 199 ± 11 nm to 208 ± 9 nm and 216 ± 10 nm, respectively, with corresponding shell thicknesses increasing from 19 ± 1 nm to 21 ± 1 nm and 24 ± 2 nm.

Magnified TEM images of Ru/HC-1–3 revealed a homogeneous distribution of Ru nanoparticles on the hollow carbon spheres (Fig. 4g, h and S1 in the SI). For Ru/HC-1 and Ru/HC-2, very small Ru nanoparticles were uniformly dispersed over the hollow carbon supports (Fig. S1 in the SI). Interestingly, in Ru/HC-3, the Ru nanoparticles were closely packed, and the surface was almost completely covered with Ru nanoparticles (Fig. 4g). In contrast, TEM analysis of C–Ru, prepared without TA

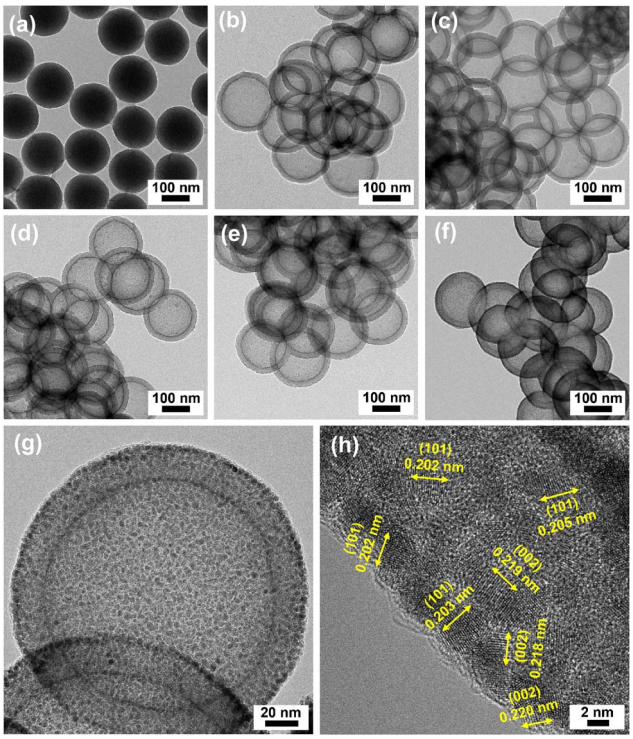

Fig. 4 TEM images of (a) SiO_2 nanospheres, (b) HMOP, (c) HMOP@TA, (d) Ru/HC-1, (e) Ru/HC-2, and (f and g) Ru/HC-3. (h) HR-TEM image of Ru/HC-3.

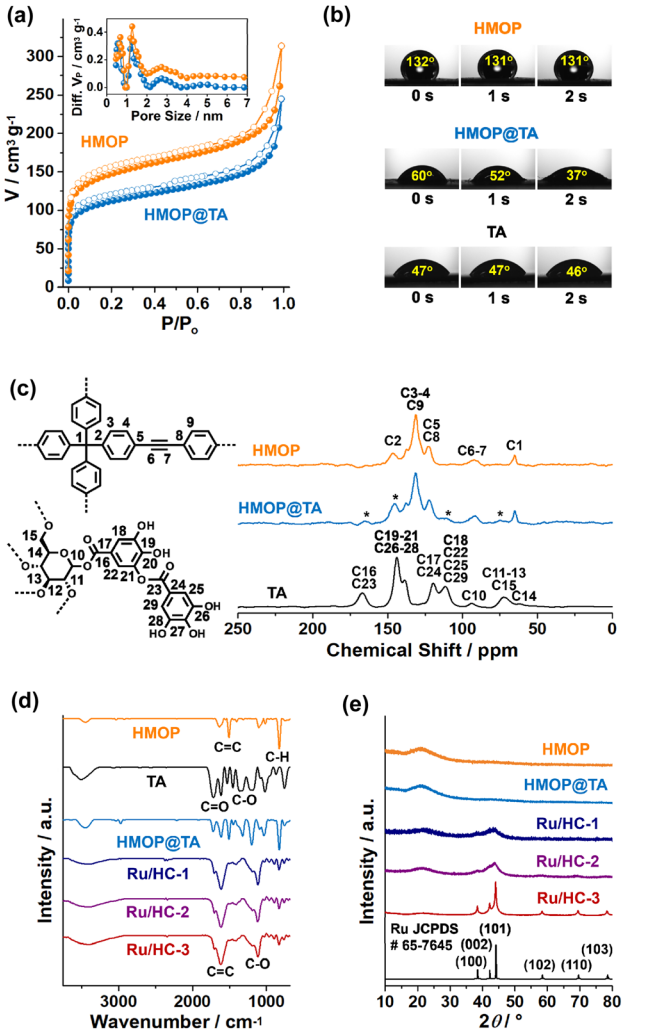

Fig. 5 (a) N_2 adsorption–desorption isotherm curves of HMOP and HMOP@TA measured at 77 K (inset: pore size distribution diagrams based on the NL-DFT method). (b) Water contact angles of the pellets of HMOP, HMOP@TA, and TA. (c) Solid state ^{13}C NMR spectra of HMOP, HMOP@TA, and TA. (d) IR spectra of HMOP, TA, HMOP@TA, and Ru/HC-1–3. (e) PXRD patterns of HMOP, HMOP@TA, and Ru/HC-1–3.

modification, showed a mixture of Ru aggregates and hollow carbon materials (Fig. S2 in the SI), indicating that TA on the surface of HMOP is critical for the efficient incorporation and uniform distribution of Ru ions.

HR-TEM analysis of Ru nanoparticles in Ru/HC-1–3 primarily revealed the (002) and (101) crystalline planes of hexagonal close-packed (hcp) metallic Ru (JCPDS #65-7645) with interplanar spacing distances of 0.213–0.218 and 0.202–0.206 nm, respectively (Fig. 4h and S3 in the SI).[10a] In addition, a minor contribution from the (100) plane was also observed, with interplanar distances of 0.232–0.234 nm (Fig. S3 in the SI). EDS-based elemental mapping studies of Ru/HC-3 revealed the distributions of Ru and C elements in the outer and inner parts of materials, respectively, indicating the successful loading of Ru on the HC materials (Fig. S4 in the SI).

The surface area and porosity of HMOP and HMOP@TA were evaluated by N_2 adsorption–desorption measurements. Both materials showed IUPAC type-I isotherms, indicating their microporous nature. HMOP exhibited a BET theory-based surface area (S_{BET}) of 544 $m^2\ g^{-1}$ and a micropore volume (V_m) of 0.13 $cm^3\ g^{-1}$, whereas HMOP@TA showed a significantly reduced S_{BET} of 415 $m^2\ g^{-1}$ and V_m of 0.10 $cm^3\ g^{-1}$, indicating the successful incorporation of TA into the micropores of HMOP (Fig. 5a and Table S2 in the SI).

To investigate the chemical properties of HMOP after TA treatment, WCAs were measured (Fig. 5b). HMOP exhibited a WCA of 132°, indicating a hydrophobic surface, whereas HMOP@TA showed a significantly reduced WCA of 60°, suggesting a change from hydrophobic to hydrophilic behavior. Furthermore, a water droplet was rapidly absorbed into HMOP@TA, with the WCA decreasing from 60° to 37° within 2 s, whereas absorption in HMOP was much slower (Fig. 5b). As a control, a TA pellet exhibited a WCA of 47°, which did not change significantly over 2 s. The facilitated water adsorption in HMOP@TA can be attributed to its hollow structure combined with the hydrophilic TA coating. These results suggest that an aqueous $RuCl_3$ precursor solution can be efficiently adsorbed into HMOP@TA.

The chemical structures of HMOP and HMOP@TA were characterized by solid-state ^{13}C NMR and IR spectroscopy. The ^{13}C NMR spectrum of HMOP exhibited peaks at 65, 92, and 122–146 ppm, corresponding to benzylic carbons, internal alkynes, and aromatic carbons, respectively, confirming the formation of MOP networks *via* the coupling of the organic

building blocks used in the synthesis (Fig. 5c). In comparison, HMOP@TA displayed three additional peaks at 74, 111, and 166 ppm, attributable to aliphatic carbons in glucose moieties, aromatic carbons in galloyl groups, and carbonyl carbons of TA, respectively (Fig. 5c).[29]

The IR spectrum of HMOP showed characteristic vibration peaks at 1509 and 824 cm^{-1}, corresponding to aromatic C=C and C–H vibrations, respectively (Fig. 5d).[30] For HMOP@TA, additional peaks appeared at 1718 (C=O), 1616 (C=O), 1324 (C–O), and 1200 (C–O) cm^{-1}, assigned to vibrations of TA.[31] In contrast, the IR spectra of Ru/HC-1–3 exhibited peaks at 1610 and 1109 cm^{-1}, corresponding to graphitic C=C and defective C–O vibrations of carbon materials, respectively (Fig. 5d).[10a]

PXRD studies indicated that both HMOP and HMOP@TA are amorphous, matching the amorphous features of the Sonogashira coupling-based MOP and TA powders reported in the literature.[32,33] In contrast, Ru/HC-3 exhibited diffraction peaks at 2θ of 38.4, 42.2, 44.1, 58.4, 69.5, and 78.5°, corresponding to the (100), (002), (101), (102), (110), and (103) planes of metallic Ru (JCPDS #65-7645) (Fig. 5e). These PXRD peaks were significantly broadened in Ru/HC-1 and Ru/HC-2, suggesting that the Ru nanoparticles in these samples are smaller than those in Ru/HC-3.

The physical and chemical properties of Ru/HC-1–3 were further characterized by various analytical techniques (Fig. 6). First, by N_2 adsorption–desorption studies, the S_{BET} of Ru/HC-1, Ru/HC-2, and Ru/HC-3 were measured to be 407, 351, and 243 $m^2\ g^{-1}$, respectively, with corresponding V_m of 0.11, 0.10, and 0.068 $cm^3\ g^{-1}$ (Fig. 6a, S5, and Table S2 in the SI). In addition, the total pore volumes (V_t) of Ru/HC-1, Ru/HC-2, and Ru/HC-3 were measured to be 0.25, 0.21, and 0.15 $cm^3\ g^{-1}$, respectively. The gradual decrease in the surface areas and pore volumes for Ru/HC-2 and Ru/HC-3, compared to those of Ru/HC-1, can be attributed to the higher Ru contents in these materials. Combustion elemental analysis indicated that with increasing of Ru contents, the total contents of C, N, O, and H in Ru/HC-1, Ru/HC-2, and Ru/HC-3 gradually decreased to be 76.0, 65.6, and 41.6 wt%, respectively. TGA in air indicated 28.5, 44.5, and 68.0 wt% residues for Ru/HC-1, Ru/HC-2, and Ru/HC-3, respectively, corresponding to 21.6, 33.8, and 51.6 wt% Ru (Fig. 6b). It is noteworthy that metallic Ru is poorly soluble in aqua regia,[22] and thus, TGA in air has been used for quantitative analysis of Ru in carbon materials.[23] By HR-TEM analysis, the average sizes of Ru nanoparticles in Ru/HC-1, Ru/HC-2, and Ru/HC-3 were statistically measured to be 1.99 ± 0.43, 2.42 ± 0.45, and 4.53 ± 0.53 nm, respectively (Fig. 6c).

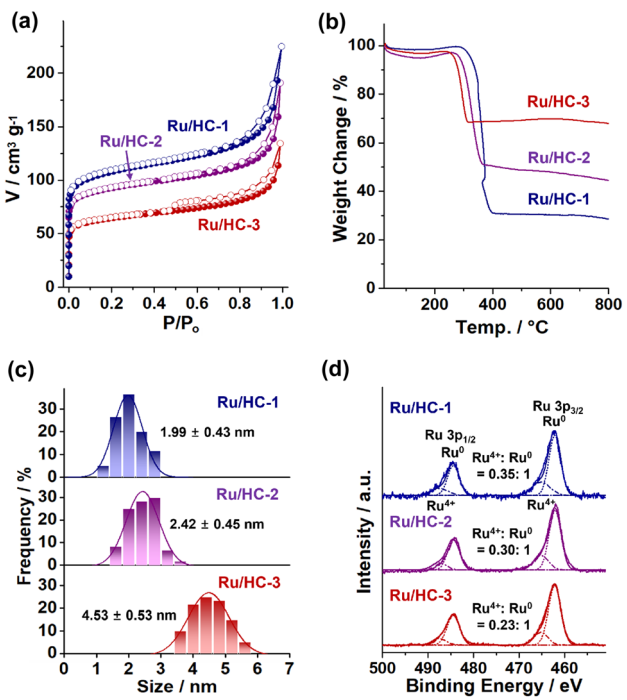

Fig. 6 (a) N_2 adsorption–desorption isotherm curves measured at 77 K, (b) TGA curves under air, (c) size distribution diagrams of Ru nanoparticles, and (d) XPS Ru 3p orbital peaks of Ru/HC-1–3.

The chemical environments of Ru in Ru/HC-1–3 were further investigated by XPS studies. The Ru $3p_{1/2}$ and $3p_{3/2}$ orbital peaks of Ru/HC-1–3 were observed at 484.4–484.5 and 462.0–462.2 eV, respectively, consisting of metallic Ru(0) and surface Ru(IV) species (Fig. 6d).[9a] As the Ru nanoparticle size increased, the ratio of Ru(IV) to Ru(0) decreased from 0.35 : 1 (Ru/HC-1) to 0.30 : 1 (Ru/HC-2) and 0.23 : 1 (Ru/HC-3), indicating that the relative portion of surface RuO_x to metallic Ru diminished with increasing particle size (Fig. 6d and S6 in the SI).[9a]

Next, we studied the catalytic performance of Ru/HC-1–3 for the conversion of LA to GVL under mild conditions (100 °C, 5 bar H_2). Table 1 and Fig. 7 and S7, S8 in the SI summarize the results. In the absence of a catalyst, no conversion of LA to GVL was observed at 100 °C under 5 bar H_2 (entry 1 in the Table 1). Using Ru/HC-1 (0.25 mol% Ru relative to LA), the conversion of LA gradually increased with reaction time: 3, 7, 11, and 16% after 0.5, 1, 2, and 3 h, respectively, while corresponding GVL yields were 2, 5, 9, and 14% at 100 °C under 5 bar H_2 (entries 2–5 in the Table 1). Ru/HC-2 (0.25 mol% Ru relatively to LA) showed higher activity, with LA conversions of 13, 28, 45, and 57% and GVL yields of 10, 25, 42, and 53% after 0.5, 1, 2, and 3 h, respectively (entries 6–9 in the Table 1).

In comparison, Ru/HC-3 (0.25 mol% Ru relative to LA) exhibited excellent catalytic performance for the conversion of LA to GVL. With increasing reaction time from 0.5 to 1 and 2 h, LA conversions increased from 55 to 80 and 100% and the corresponding GVL yields increased from 38 to 67 and 94% at 100 °C under 5 bar H_2 (entries 10–12 in the Table 1). Interestingly, 4-hydroxypentanoic acid (HPA) was formed with a yield of 17% after 0.5 h, which gradually decreased to 13 and 6% after 1 and 2 h. Extending the reaction time to 3 h did not significantly change the yields of GVL or HPA (entry 13 in the Table 1).

When the reaction temperature was decreased to 80 and 60 °C, LA conversions dropped to 63 and 44%, with GVL yields of 46 and 32%, respectively (entries 14 and 15 in the Table 1). Similarly, lowering the H_2 pressure to 3 and 1 bar reduced LA conversions to 71 and 2%, respectively, with GVL yields of 66 and 2% (entries 16 and 17 in the Table 1). Based on these results, the optimal catalytic system was determined to be Ru/HC-3 (0.25 mol% Ru relative to LA) at 100 °C and 5 bar H_2 for

Table 1 Conversion of LA to GVL catalyzed by Ru/HC-1 (Ru1), Ru/HC-2 (Ru2), Ru/HC-3 (Ru3), and control Ru/C (C–Ru)[a]

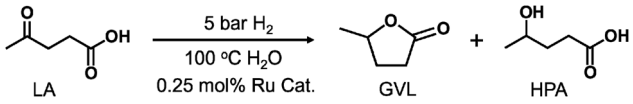

Entry	Cat.	P_{H_2} (bar)	T (°C)	Time (h)	Conv.[b] (%)	GVL[c] (%)	HPA[c] (%)
1	—	5	100	2	0	0	0
2	Ru1	5	100	0.5	3	2	1
3	Ru1	5	100	1	7	5	2
4	Ru1	5	100	2	11	9	2
5	Ru1	5	100	3	16	14	2
6	Ru2	5	100	0.5	13	10	3
7	Ru2	5	100	1	28	25	3
8	Ru2	5	100	2	45	42	3
9	Ru2	5	100	3	57	53	4
10	Ru3	5	100	0.5	55	38	17
11	Ru3	5	100	1	80	67	13
12	Ru3	5	100	2	100	94 (91)	6
13	Ru3	5	100	3	100	94	6
14	Ru3	5	80	2	63	46	17
15	Ru3	5	60	2	44	32	12
16	Ru3	3	100	2	71	66	5
17	Ru3	1	100	2	2	2	0
18	C–Ru	5	100	0.5	25	21	4
19	C–Ru	5	100	1	40	35	5
20	C–Ru	5	100	2	40	37	3
21	C–Ru	5	100	3	40	37	3
22[d]	Ru3	5	100	2	100	92	8
23[e]	Ru3	5	100	2	100	91	9
24[f]	Ru3	5	100	2	100	92	8
25[g]	Ru3	5	100	2	100	93	7

[a] Reaction conditions: LA (2.0 mmol), catalyst (0.25 mol% Ru relative to LA, 2.14 mmol Ru per g in Ru1, 3.34 mmol Ru per g in Ru2, 5.11 mmol Ru per g in Ru3, 4.94 mmol Ru per g in C–Ru), H_2O (2 mL). [b] Conversion yields of LA. [c] Yields of GVL and HPA (maleic acid was used as an internal standard and the isolated yield is given in parenthesis). [d] The catalyst recovered from entry 12 was used. [e] The catalyst recovered from entry 22 was used. [f] The catalyst recovered from entry 23 was used. [g] The catalyst recovered from entry 24 was used.

2 h, yielding an isolated GVL of 91% (entry 12 in the Table 1; Fig. S8 in the SI).

Compared to Ru/HC-3, the control catalyst C–Ru (0.25 mol% Ru relative to LA), prepared using HMOP templates without TA coating, exhibited poor catalytic performance (Fig. S2 in the SI; entries 18–21, Table 1). The Ru nanoparticles in C–Ru displayed a broad and uncontrolled size distribution, with an average size of 6.70 ± 4.24 nm (Fig. S2 in the SI). Although the Ru content (49.9 wt%) and S_{BET} (273 $m^2\ g^{-1}$) of C–Ru were comparable to those of Ru/HC-3, its catalytic activity was significantly lower. With C–Ru, increasing the reaction time from 0.5 to 1 h increased the LA conversion from 25 to 40% and the GVL yield from 21 to 35%. However, further extension of the reaction time to 2 and 3 h did not enhance the conversion. The poor performance of C–Ru is attributed to the uncontrolled aggregation of Ru nanoparticles.

The reaction pathways for the conversion of LA to GVL catalyzed by Ru/HC-3 are proposed in Fig. 7a.[8,9] Under the reductive conditions of H_2, the RuO_x surface species of Ru nanoparticles can be reduced to zerovalent metallic Ru. H_2 reacts with the zerovalent Ru to form Ru-hydride species in a LA* + 2H* intermediate *via* the conventional oxidative addition. After coordination of LA to the Ru surface, the hydride attacks the carbonyl group of LA through migratory insertion to form a LAH* + H* intermediate. The resulting alkoxy species of the LAH* subsequently attacks the carboxylic acid group, leading to OH elimination and the formation of a GVL* + OH* + H* intermediate, as illustrated in sequential pathway A in Fig. 7a. During this process, the hydride and hydroxo ligands generate water through reductive elimination.

Alternatively, the reductive elimination of alkoxy and hydride ligands of the LAH* + H* intermediate structure can produce a HPA* intermediate. Conversion of HPA to GVL proceeds *via* oxidative addition of the OH group of HPA to form alkoxy and hydride ligands, as indicated in stepwise pathway B.

To gain mechanistic insight into the sequential pathway A and the stepwise pathway B involving the formation of HPA during the conversion of LA to GVL, density functional theory (DFT) calculations were conducted using the Vienna *Ab initio* Simulation Package (VASP)[25] (Fig. 7b, S9, S10, and Table S3 in the SI). The Ru(002) surface was modeled by optimizing the Ru unit cell, which yielded lattice parameters of $a = b = 2.71$ Å, consistent with reported values.[34] The reaction of LA and H_2 on the Ru(002) surface yielded sequential intermediates, LA* + H_2^*,

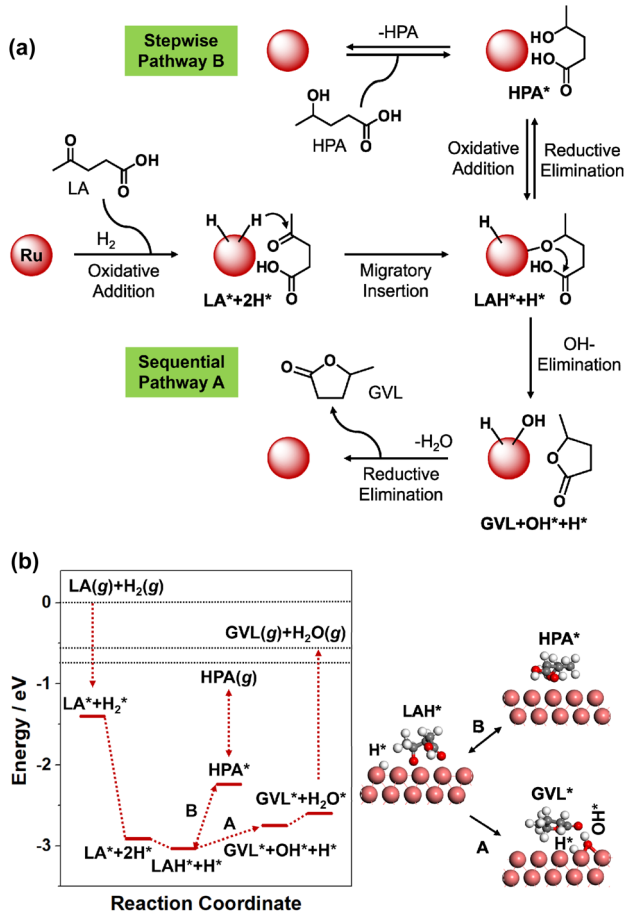

Fig. 7 (a) Ru-catalyzed reaction pathways for the conversion of LA to GVL. (b) DFT-calculated energy profiles of intermediate structures, reactants, and products in the reaction pathways and DFT-optimized structures of key reaction intermediates: LAH* + H*, HPA*, and GVL* + OH* + H*.

LA* + 2H*, and LAH* + H*, with energy stabilizations of −1.40, −2.91, and −3.03 eV, respectively, relative to LA(g) + H_2(g) substrates. The substantial stabilization observed for LAH* + H* suggests that the initial hydrogenation step on the Ru(002) surface is thermodynamically favorable and effectively promotes the conversion of LA. The formation of the HPA* intermediate requires an additional energy of +0.79 eV, whereas the conversion to the GVL* + OH* + H* intermediate occurs with a comparatively lower energy of +0.28 eV. The following step, leading to the formation of GVL* + H_2O* from GVL* + OH* + H*, involves only a small energy of +0.15 eV, indicating facile water formation and product stabilization. These energy profiles clearly indicate that the sequential path A is more favorable than the stepwise path B, and that HPA likely serves as a transient yet significant surface-bound intermediate. This HPA intermediate exhibits a strong interaction with the Ru(002) surface, showing a stabilization energy of −2.24 eV relative to LA(g) + H_2(g). This close interaction enables the hydroxyl group of HPA to undergo oxidative addition with surface Ru atoms, regenerating the LAH* + H* intermediate with an energy gain of −0.79 eV.

The binding energies of LA, HPA, and GVL were calculated to be −1.30, −1.39, and −1.24 eV, respectively, indicating that both LA and HPA interact strongly with the Ru(002) surface, promoting efficient surface reactions, while the weaker binding of GVL facilitates its desorption and completes the catalytic cycle. These results further support the proposed mechanism, confirming that the Ru(002) surface effectively stabilizes key intermediates and promotes the sequential conversion pathway from LA to GVL through the formation of HPA as a reactive intermediate.

To understand the excellent catalytic performance of Ru/HC-3 under mild conditions, compared to those of Ru/HC-1–2, TPR studies were conducted under H_2 (Fig. 8a). Interestingly, as the Ru loading increased from Ru/HC-1 to Ru/HC-2 and Ru/HC-3, the first reduction temperature in the H_2-TPR profiles gradually decreased from 94–118 °C to 91 and 80 °C, respectively. It has been well reported that the surface of Ru nanoparticles is partially oxidized to form RuO_x species upon air exposure and that the first reduction peaks correspond to the reduction of these surface RuO_x species.[35] The reduction of surface RuO_x species by H_2 gas proceeds by oxidative addition of H_2, followed by the generation of water (Fig. 8c).[35] In comparison, the second

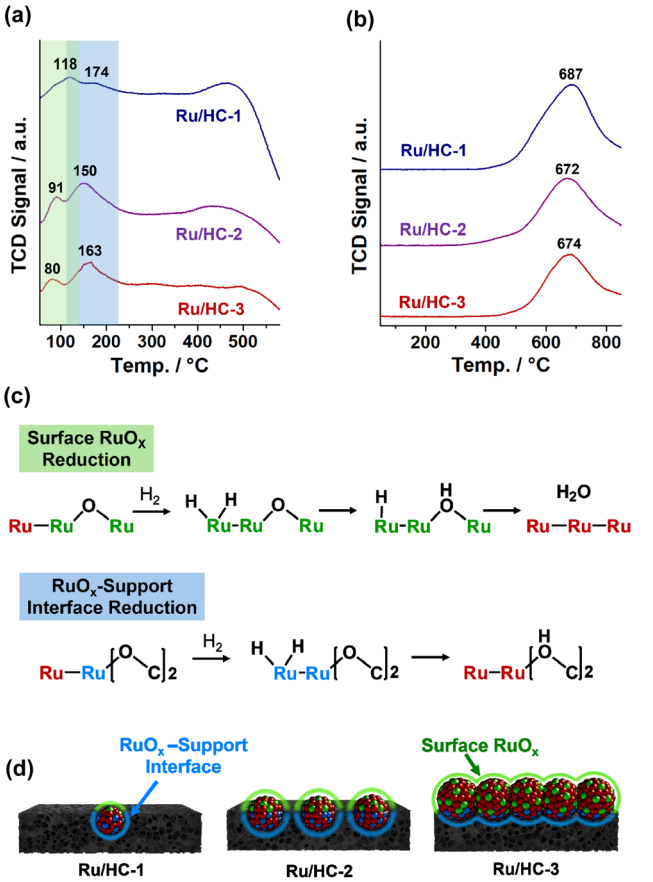

Fig. 8 (a) H_2-TPR and (b) H_2-TPD profiles of Ru/HC-1–3. (c) H_2-induced reduction processes of RuO_x species on the surface and at the interface with carbon supports. (d) Comparative illustration of the surface RuO_x species and the RuO_x–support interfaces in the Ru/HC-1–3.

reduction peaks of Ru/HC-1, Ru/HC-2, and Ru/HC-3 were observed at higher temperatures of 174, 150, and 163 °C, respectively, corresponding to the reduction of RuO_x species located at the carbon–Ru interface (Fig. 8a and c).[35] H_2-TPD profiles of Ru/HC-1–3 showed desorption temperatures of 687, 672, and 674 °C, respectively (Fig. 8b). These results indicate that Ru/HC-1–3 interact efficiently with H_2 and that the predominant surface RuO_x species of Ru/HC-3 (Ru–O–Ru : Ru–O–X = 1 : 0.65 based on the XPS analysis of O 1s orbital peaks, X = H or C) can be efficiently reduced to zerovalent Ru under mild temperature condition (80 °C), generating catalytically active Ru species (Fig. 8d and S6 in the SI). In comparison, the major RuO_x–carbon interface species of Ru/HC-1 (Ru–O–Ru : Ru–O–X = 1 : 7.35 based on the XPS analysis of O 1s orbital peaks, X = H or C) are hardly reducible at temperature of 100 °C (Fig. 8d and S6 in the SI), which can account for the superior catalytic performance of Ru/HC-3, compared to Ru/HC-1–2, under mild reaction conditions.

The recyclability of Ru/HC-3 as a heterogeneous catalyst was evaluated for the conversion of LA to GVL (Fig. 9). Under the optimized reaction conditions (0.25 mol% Ru relative to LA, 5 bar H_2, 100 °C, 2 h), Ru/HC-3 exhibited excellent recyclability, maintaining complete LA conversion and GVL yields of 91–94% over five successive runs (Fig. 9a and S11 in the SI; entries 12 and 22–25 in the Table 1). When Ru/HC-3 was removed from the reaction mixture by filtration after 0.5 h, the reaction actually ceased at 55–56% conversions of LA during the next 1.5 h, confirming the heterogeneous nature of the catalytic system (Fig. 9b). Homogeneous Ru species in the reaction mixture were not detected by ICP-AES analysis, indicating that Ru was not leached from Ru/HC-3.

TEM analysis of Ru/HC-3 recovered after five successive recycle runs showed complete retention of the original nanoparticulate feature of Ru materials and the hollow morphology of carbon spheres (Fig. 9c–e). PXRD and IR analysis of the recovered catalyst confirmed the preservation of the original metallic Ru phase and chemical structure of Ru/HC-3 (Fig. 9f and S12 in the SI). XPS studies of the Ru $3p_{1/2}$ and $3p_{3/2}$ orbitals revealed a decrease in the Ru(IV) : Ru(0) ratio from the original 0.23 : 1 to 0.11 : 1 (Fig. 9g and S13 in the SI), which is attributed to the reductive environment of H_2 and the partial reduction of surface RuO_x species.[36] Analysis of the Ru content in the recovered Ru/HC-3 indicated only a slight decrease from the original 51.6 wt% to 48.1 wt%, possibly due to the entrapment of organic residues within the micropores.

The catalytic performance of Ru/HC-3 was compared with those of Ru-based heterogeneous catalysts reported in the literature (Table S1 in the SI).[8–10] Various Ru-based catalysts have been developed for the conversion of LA to GVL, typically containing 0.37–5 wt% Ru loaded on solid supports such as carbons, SiO_2, Al_2O_3, TiO_2, and ZrO_2.[8,9] These catalysts generally operate with 0.25–2.8 mol% Ru for LA at high temperatures (120–190 °C) and high H_2 pressures (35–50 bar).[8,9] For example, Corma and coworkers reported 0.6 wt% Ru/TiO_2, which achieved a 93% GVL yield with 0.4 mol% Ru for LA after 5 h at 150 °C under 35 bar H_2, corresponding to a TON of 232.5 and a TOF of 46.6 h^{-1}.[8a] Lu and coworkers employed Ru nanoparticles

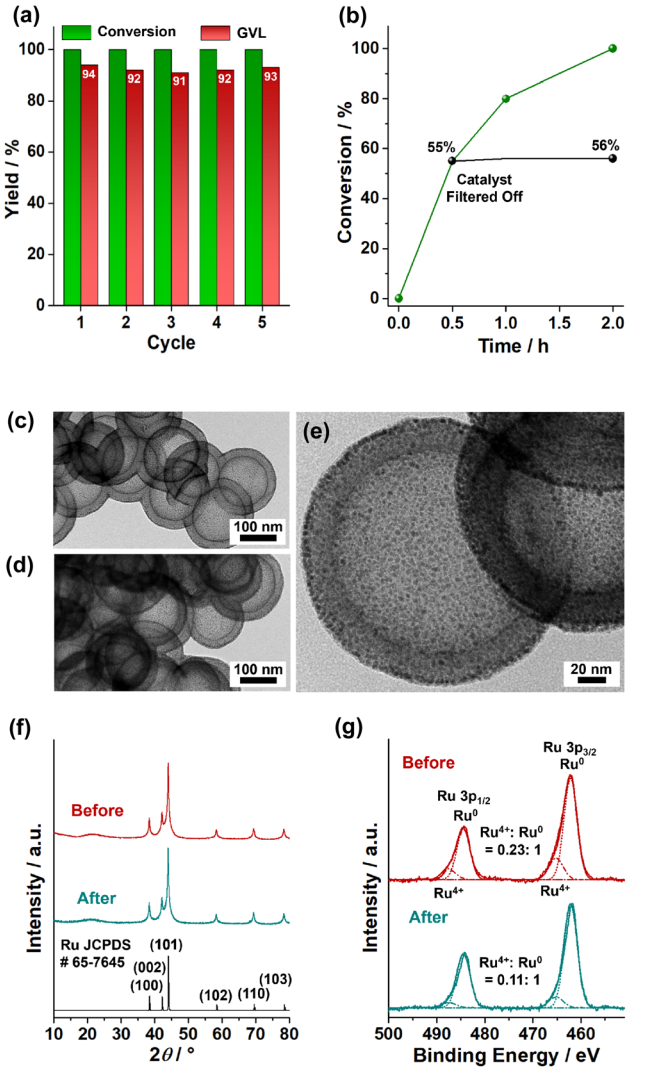

Fig. 9 (a) Recyclability of Ru/HC-3 for the conversion of LA to GVL (reaction conditions: 0.25 mol% Ru, 2.0 mmol LA, 5 bar H_2, 2 mL H_2O, 100 °C, 2 h). (b) Filtration test of Ru/HC-3 during the reaction (catalyst removed after 0.5 h). TEM images of Ru/HC-3 (c) before and (d and e) after five successive runs. (f) PXRD patterns and (g) XPS Ru 3p spectra of Ru/HC-3 before and after five successive reactions.

confined within hollow carbon spheres, obtaining a 92.74% GVL yield after 4 h at 180 °C under 40 bar H_2, with a TON of 545.5 and a TOF of 136.4 h^{-1}.[8b] Recently, Chen and coworkers reported 4.8 wt% Ru/Al_2O_3, which provided an 88.9% GVL yield with 1.84 mol% Ru for LA after 4 h at 190 °C under 50 bar H_2, corresponding to a TON of 48.3 and a TOF of 12.1 h^{-1}.[8c] For the production of GVL under H_2 pressure free conditions, alternative hydrogen sources such as isopropanol or formic acid have been employed in Ru-based catalytic systems.[10] However, these systems typically require 1–2.8 mol% Ru for LA and elevated temperatures (120–150 °C), resulting in relatively low TONs (33–99) and TOFs (11–66 h^{-1}).[10]

In this context, the catalytic performance of Ru/HC-3 (0.25 mol% Ru for LA) is highly promising, achieving a TON of 376 and a TOF of 188 h^{-1} for the conversion of LA to GVL at

100 °C under 5 bar H_2. The compact nanoparticulate structure of Ru on hollow carbon supports likely enhances substrate interactions and facilitates the tandem conversion of LA to GVL, owing to the high density of active sites on the catalyst surface. In addition, the excellent catalytic performance of Ru/HC-3 under mild conditions is attributable to the facile reduction of surface RuO_x species at the mild temperature of 80 °C. While the TPR temperatures of surface RuO_x species in the Ru-based catalysts have typically been reported in the range of 95–250 °C (Table S4 in the SI),[8c,35,37] it is noteworthy that Ru/HC-3 exhibited an unusually low TPR temperature of 80 °C.

Conclusions

This work shows the development of Ru/HC-based efficient heterogeneous catalysts for the conversion of LA to GVL under mild conditions. TA-coated HMOP was employed as a template for the fabrication of Ru/HC catalysts. With the aid of TA networks, well-controlled Ru/HC catalysts with high Ru loadings (up to 51.6 wt%) and compact nanoparticulate structures were obtained. The optimized Ru/HC-3 (0.25 mol% Ru relative to LA) achieved complete conversion of LA with a 94% yield of GVL in 2 h at 100 °C under 5 bar H_2, corresponding to a TON of 376 and a TOF of 188 h^{-1}. The excellent catalytic performance of Ru/HC-3 in the conversion of LA and HPA intermediate to GVL under ambient conditions, compared with Ru/HC-1–2, is attributable to the facile reduction of the surface RuO_x species. We believe that the synthetic strategy of this work could be extended to load other metals onto hollow carbon supports for various biomass conversion reactions.

Author contributions

S. U. Son and J. Y. Lee: conceptualization, supervision, writing – original draft, and review and editing. Y. S. Kong, R. Parida, Y. K. Kim and H. S. Kim: investigation and formal analysis.

Conflicts of interest

There are no conflicts to declare.

Data availability

The data supporting this article have been included as part of the supplementary information (SI). Supplementary information: additional TEM, HR-TEM, EDS-mapping images, additional characterization data of C–Ru, Ru/HC-1–3, and recovered Ru/HC-3, NMR spectra of reaction mixtures and an isolated GVL, additional DFT calculation results, and catalytic performance comparison table. See DOI: https://doi.org/10.1039/d5ta09104g.

Acknowledgements

This work was supported by the Carbon Upcycling Project for Platform Chemicals (no. RS-2022-NR068679) and by the National Research Foundation of Korea (NRF) grants (no. RS-2023-00208797) funded by the Korea government (MSIT).

References

1 K. Lee, Y. Jing, Y. Wang and N. Yan, *Nat. Rev. Chem.*, 2022, **6**, 635–652.
2 A. D. Dwivedi, B. Priya, R. Chinthala, D. S. Pandey and S. K. Singh, *Tetrahedron Green Chem*, 2023, **1**, 100008.
3 (*a*) F. J. A. G. Coumans, Z. Overchenko, J. J. Wiesfeld, N. Kosinov, K. Nakajima and E. J. M. Hensen, *ACS Sustainable Chem. Eng.*, 2022, **10**, 3116–3130; (*b*) L. Huai, J. Zhang and W. A. Goddard III, *J. Am. Chem. Soc.*, 2024, **146**, 31251–31263; (*c*) R. Guo, Y. Zeng, L. Lin, D. Hu, C. Lu, S. Conroy, S. Zhang, C. Zeng, H. Luo, Z. Jiang, X. Zhang, X. Tu and K. Yan, *Angew. Chem., Int. Ed.*, 2025, **64**, e202418234.
4 E. M. El-Fawal, A. M. A. El-Naggar, A. A. El-Zahhar, M. M. Alghandi, A. S. Morshedy, H. A. El-Sayed and A. S. M. E. Mohammed, *RSC Adv.*, 2025, **15**, 11942–11974.
5 H. Xia, S. Xu, H. Hu, J. An and C. Li, *RSC Adv.*, 2018, **8**, 30875–30886.
6 M. Sajid, U. Farooq, G. Bary, M. M. Azim and X. Zhao, *Green Chem.*, 2021, **23**, 9198–9238.
7 W.-P. Xu, X.-F. Chen, H.-J. Guo, H.-L. Li, H.-R. Zhang, L. Xiong and X.-D. Chen, *J. Chem. Technol. Biotechnol.*, 2021, **96**, 3009–3024.
8 (*a*) A. Primo, P. Concepcion and A. Corma, *Chem. Commun.*, 2011, **47**, 3613–3615; (*b*) Z. Yu, N. Ji, J. Xiong, X. Li, R. Zhang, L. Zhang and X. Lu, *Angew. Chem., Int. Ed.*, 2021, **60**, 20786–20794; (*c*) Y. Liu, C. Gu, L. Chen, W. Zhou, Y. Liao, C. Wang and L. Ma, *ACS Appl. Mater. Interfaces*, 2023, **15**, 4184–4193.
9 (*a*) Z. Wei, J. Lou, C. Su, D. Guo, Y. Liu and S. Deng, *ChemSusChem*, 2017, **10**, 1720–1732; (*b*) A. S. Piskun, J. E. de Haan, E. Wilbers, H. H. Van de Bovenkamp, Z. Tang and H. J. Heeres, *ACS Sustainable Chem. Eng.*, 2016, **4**, 2939–2950; (*c*) M. Nemanashi, J.-H. Noh and R. Meijboom, *Appl. Catal., A*, 2018, **550**, 77–89; (*d*) H. C. Genuino, H. H. van de Bovenkamp, E. Wilbers, J. G. M. Winkelman, A. Goryachev, J. P. Hofmann, E. J. M. Hensen, B. M. Weckhuysen, P. C. A. Bruijnincx and H. J. Heeres, *ACS Sustainable Chem. Eng.*, 2020, **8**, 5903–5919.
10 (*a*) C. V. Nguyen, A. H. N. Duong and N. D. Q. Chau, *ChemistrySelect*, 2024, **9**, e202403391; (*b*) T. T. Nguyen, D. D. V. Ngoc, H. T. Lai, A. T. T. Pham, B. M. Matsagar, K. C.-W. Wu and C. V. Nguyen, *ChemCatChem*, 2025, **17**, e202500271; (*c*) E. V. Sanchez, J. F. J. Tzompantzi-Morales, L. Ortiz-Frade, M. Esparza-Schulz, R. Ojeda-Lopez, R. Perez-Hernandez, A. Gutierrez-Carrillo, L. Huerta, V. H. Lara, L. Lomas-Romero and L. Gonzalez-Sebastian, *Dalton Trans.*, 2025, **54**, 4201–4212.
11 (*a*) S. Mondal, S. Ruidas, S. Chongdar, B. Saha and A. Bhaumik, *ACS Sustainable Chem. Eng.*, 2024, **1**, 1672–1704; (*b*) L. Lin, X. Han, B. Han and S. Yang, *Chem. Soc. Rev.*, 2021, **50**, 11270–11292.
12 Y. Liu, J. Goebl and Y. Yin, *Chem. Soc. Rev.*, 2013, **42**, 2610–2653.

13 G. Prieto, H. Tuysuz, N. Duychaerts, J. Knossalla, G. H. Wang and F. Schuth, *Chem. Rev.*, 2016, **116**, 14056–14119.
14 J.-S. M. Lee and A. I. Cooper, *Chem. Rev.*, 2020, **120**, 2171–2214.
15 H. S. Lee, J. Choi, J. Jin, J. Chun, S. M. Lee, H. J. Kim and S. U. Son, *Chem. Commun.*, 2012, **48**, 94–96.
16 K. Cho, C. W. Kang, S. H. Ryu, J. Y. Jang and S. U. Son, *J. Mater. Chem. A*, 2022, **10**, 6950–6964.
17 N. Kang, J. H. Park, J. Choi, J. Jin, J. Chun, I. G. Jung, J. Jeong, J.-G. Park, S. M. Lee, H. J. Kim and S. U. Son, *Angew. Chem., Int. Ed.*, 2012, **51**, 6626–6630.
18 M. Hosseini, L. Moghaddam, L. Barner, S. Cometta, D. W. Hutmacher and F. M. Savi, *Prog. Polym. Sci.*, 2025, **160**, 101908.
19 C. Chen, H. Yang, X. Yang and Q. Ma, *RSC Adv.*, 2022, **12**, 7689–7711.
20 (*a*) H. Ejima, J. J. Richardson, K. Liang, J. P. Best, M. P. van Koeverden, G. K. Such, J. Cui and F. Caruso, *Science*, 2013, **341**, 154–157; (*b*) J. Guo, Y. Ping, H. Ejima, K. Alt, M. Meissner, J. J. Richardson, Y. Yan, K. Peter, D. von Elverfeldt, C. E. Hagemeyer and F. Caruso, *Angew. Chem., Int. Ed.*, 2014, **53**, 5546–5551; (*c*) T. Liu, M. Zhang, W. Liu, X. Zeng, X. Song, X. Yang, X. Zhang and J. Feng, *ACS Nano*, 2018, **12**, 3917–3927.
21 W. Stober, A. Fink and E. Bohn, *J. Colloid Interface Sci.*, 1968, **26**, 62–69.
22 (*a*) L. Sandig-Predzymirska, T. V. Barreiros, A. Weigelt, S. Pitscheider, C. M. Pedersen, C. Kallesoe, A. Thiere, M. Stelter and A. Charitos, *J. Sustain. Metall.*, 2025, **11**, 145–159; (*b*) J.-C. Zhang, B.-H. Ge, T.-F. Liu, Y.-Z. Yang, B. Li and W.-Z. Li, *ACS Catal.*, 2020, **10**, 783–791.
23 D. H. Kweon, M. S. Okyay, S.-J. Kim, J.-P. Jeon, H.-J. Noh, N. Park, J. Mahmood and J.-B. Baek, *Nat. Commun.*, 2020, **11**, 1278.
24 T. Mitsudome, A. Noujima, T. Mizugaki, K. Jisukawa and K. Kaneda, *Green Chem.*, 2009, **11**, 793–797.
25 G. Kresse and D. Joubert, *Phys. Rev. B: Condens. Matter Mater. Phys.*, 1999, **59**, 1758–1775.
26 P. E. Blöchl, *Phys. Rev. B: Condens. Matter Mater. Phys.*, 1994, **50**, 17953–17979.
27 S. Grimme, J. Antony, S. Ehrlich and H. Krieg, *J. Chem. Phys.*, 2010, **132**, 154104.
28 N. Kang, J. H. Park, M. Jin, N. Park, S. M. Lee, H. J. Kim, J. M. Kim and S. U. Son, *J. Am. Chem. Soc.*, 2013, **135**, 19115–19118.
29 C. Chen, X. Yang, S.-J. Li, C. Zhang, Y.-N. Ma, Y.-X. Ma, P. Gao, S.-Z. Gao and X.-J. Huang, *Green Chem.*, 2021, **23**, 1794–1804.
30 Y. K. Kim, S. L. Park, J. D. Lee and S. U. Son, *J. Mater. Chem. A*, 2024, **12**, 31825–31832.
31 Y. Fang, J. Tan, H. Choi, S. Lim and D.-H. Kim, *Sens. Actuators, B*, 2018, **259**, 155–161.
32 J.-X. Jiang, F. Su, A. Trewin, C. D. Wood, N. L. Campbell, H. Niu, C. Dickinson, A. Y. Ganin, M. J. Rossinsky, Y. Z. Khimyak and A. I. Cooper, *Angew. Chem., Int. Ed.*, 2007, **46**, 8574–8578.
33 Z. Liu, H. Fan, W. Li, G. Bai, X. Li, N. Zhao, J. Xu, F. Zhou, X. Guo, B. Dai, E. Benassi and X. Jia, *Nanoscale*, 2019, **11**, 4751–4758.
34 C. Song, O. Sakata, L. S. R. Kumara, S. Kohara, A. Yang, K. Kusada, H. Kobayashi and H. Kitagawa, *Sci. Rep.*, 2016, **6**, 31400.
35 M. Chen, L. Liu, X. Chen, X. Qin, J. Zhang, S. Xie, F. Liu, H. He and C. Zhang, *Nat. Commun.*, 2024, **15**, 9478.
36 Y. Dang, T. Wu, H. Tan, J. Wang, C. Cui, P. Kerns, W. Zhao, L. Posada, L. Wen and S. L. Suib, *Energy Environ. Sci.*, 2021, **14**, 5433–5443.
37 (*a*) Q. Lin, X. Y. Liu, Y. Jiang, Y. Wang, Y. Huang and T. Zhang, *Catal. Sci. Technol.*, 2014, **4**, 2058–2063; (*b*) Z. Yang, D. Li, L. Zhang, J. Zheng, N. Zhang and B. H. Chen, *ChemCatChem*, 2017, **9**, 338–346; (*c*) B. C. Filiz, E. S. Gnanakumar, A. Martinez-Arias, R. Gengler, P. Rudolf, G. Rothenberg and N. R. Shiju, *Chem. Lett.*, 2017, **147**, 1744–1753; (*d*) Y. Guo, S. Mei, K. Yuan, D.-J. Wang, H.-C. Liu, C.-H. Yan and Y.-W. Zhang, *ACS Catal.*, 2018, **8**, 6203–6215; (*e*) Y. Zhang, X. Su, L. Li, H. Qi, C. Yang, W. Liu, X. Pan, X. Liu, X. Yang, Y. Huang and T. Zhang, *ACS Catal.*, 2020, **10**, 12967–12975; (*f*) Y. Zhou, J. Wang, L. Liang, Q. Sai, J. Ni, C.-T. Au, X. Lin, X. Wang, Y. Zheng and L. Jiang, *J. Catal.*, 2021, **404**, 501–511.

